Future Batteries 3 (2024) 100005

Contents lists available at ScienceDirect

Future Batteries

journal homepage: www.sciencedirect.com/journal/future-batteries

Degradation of lithium-ion batteries under automotive-like conditions: aging tests, capacity loss and q-OCP interpretation

G. Sordi *, A. Rondi, D. Conti, A. Casalegno, C. Rabissi

Politecnico di Milano, Department of Energy, via Lambruschini 4, Milano 20156, Italy

ARTICLE INFO

Keywords:
Lithium-ion batteries
Degradation
Diagnostics
Driving cycle
Capacity loss

ABSTRACT

Battery electric vehicles are spreading worldwide as a relevant solution for the decarbonization of the transportation sector, ensuring high volume and weight-based energy density, high efficiency and low cost. Nevertheless, batteries are known to age in a rather complex and conditions-dependent way. This work aims at investigating battery aging resulting from close-to-real world conditions, highlighting single stressors role. Hence, aiming at representativeness for automotive application, an extensive literature review is performed, identifying a wide set of representative conditions together with their specific variations to be investigated. Realistic driving schedules like WLTP is identified and continuously applied in cycling on commercial samples, investigating the capacity loss from a q-OCP perspective with an equilibrium model. In general, loss of lithium inventory is detected as the main degradation parameter, likely related to SEI growth. Recharge C-rate and load profile appear as poorly-affecting degradation, while a dominant role is associated with operating temperature. Interestingly, temperature and cycling-related degradation appears to be independent and their effects can be effectively superimposed. Loss of active positive electrode material seems particularly affected by cycling depth of discharge, likely having mechanical origin as particle cracking.

Introduction

The spread of electric vehicles on large scale is a very recent trend. As a consequence, it is hard to find extensive databases of degradation data coming from the field. Moreover, it is common to ignore important information regarding the battery properties due to industrial property. In the academia, the role of the operating conditions is often investigated, exploiting constant-current (CC) cycles at various combinations of conditions. The limitations of these analyses are associated with the selection of the load profile and with the characterization procedure. For instance, the operation of a car is highly dynamic, differently from CC load profiles. This difference can affect the degradation path. Furthermore, residual capacity is often the only monitored degradation parameter. Previous analyses [1–4] showed how the combined use of discharge and electrochemical impedance spectroscopy (EIS) can improve the interpretation of the performance evolution of a battery. Therefore, it is expected to provide a better understanding of the ageing, too, with respect to the use of residual capacity only.

In the following, an extensive literature review is reported regarding the operating conditions that characterize the lifetime of a battery electric vehicle (BEV) battery, with a special focus on the load profile. Then, an experimental campaign is outlined accordingly and 13 battery cycling tests of several months in duration are carried out. Degradation is investigated with characterization tests, physical model simulations and ex-situ analyses. Due to the large amount of data, the residual capacity analysis is here investigated together with the evolution of thermodynamic parameters, while a wider view will be the topic of a forthcoming publication.

Literature review

After identifying the need of studying degradation in an automotive-like application, this section aims at providing an overview of the most common conditions in which a BEV battery operates. In particular, environmental temperature, state of charge window, charging C-rate and load profile are investigated in detail. Based on this review, the conditions of the experimental campaign are later selected.

Temperature

Performance, life and safety of a lithium-ion battery are highly

* Corresponding author.
E-mail address: gabriele.sordi@polimi.it (G. Sordi).

https://doi.org/10.1016/j.fub.2024.100005
Received 5 May 2024; Received in revised form 14 July 2024; Accepted 19 July 2024
Available online 25 July 2024

Nomenclature

Acronym description

BEV	Battery Electric Vehicle.
BOL	Begin of life.
BTMS	Battery thermal management system.
CADC	Common Artemis Driving Cycles.
CC	Constant current.
CEI	Cathode Electrolyte Interphase.
DoD	Depth of discharge.
DST	Dynamic Stress Test.
DV	Differential Voltage.
EFC	Equivalent Full Cycle.
EIS	Electrochemical Impedance Spectroscopy.
EV	Electric vehicle.
FUDS	Federal Urban Driving Schedule.
IEC	International Electrotechnical Commission.
LAM	Loss of Active electrode Material.
LDC	Local Driving Cycle.
LLI	Loss of Lithium Inventory.
LMO	Lithium-manganese-oxide battery.
NEDC	New European Driving Cycle.
NCA	Lithium-nickel-cobalt-aluminum-oxide battery.
NMC	Lithium-nickel-manganese-cobalt-oxide battery.
OCP	Open-Circuit Potential.
PSO	Particle Swarm Optimisation Algorithm.
SDC	Standard Driving Cycle.
SEI	Solid electrolyte interphase.
SoC	State of charge.
UDDS	Urban Dynamometer Driving Schedule.
UNECE	United Nations Economic Commission for Europe.
WLTP	World harmonized Light-duty vehicles Test Procedure.

Symbol unit of measure description latin

A	$[m^2]$, Cross-sectional area.
c	$[-]$, Coefficient.
C	$[Ah]$, Charge.
f	$[-]$, Coefficient.
F	$[N]$, Force.
g	$[ms^{-2}]$, Gravitational acceleration.
I	$[A]$, Current.
m	$[kg]$, Mass.
N	$[-]$, Number.
P	$[W]$, Power.
v	$[ms^{-1}]$, Velocity.
V	$[V]$, Voltage.
W	$[Wh]$, Cell electric energy.
X	$[h^{-1}]$, Power to Energy ratio.

Greek

α	$[^\circ]$, Inclination of the road.
Δ	$[-]$, Difference.
η	$[-]$, Efficiency.
ρ	$[-]$, Density.

Superscript

aged	Aged.
Symbol	**Unit of measure, Description.**
BoL	Begin of life.

Subscript

a	Aerodynamic.
act	Actual.
air	Air.
aux	Auxiliary.
$battery$	Battery.
BOL	Begin of life.
c	Climbing.
$cell$	Cell.
$driving$	Driving.
dt	Drivetrain.
g	Weight.
i	Inertia.
l	Load.
$loss$	Loss.
max	Maximum.
m	Motor.
nom	Nominal.
r	Rolling.
v	Vehicle.
w	Drag.

influenced by storage temperature [5,6]. It can vary either due to a varying ambient temperature or due to self-heating, due to irreversibility that occur during operation. Therefore, the temperature of the device has to be controlled, to remain in the correct operating window. A battery thermal management system (BTMS) is essential on a car, to prevent the batteries from the adverse effects caused by the rise in temperature and internal heat generation. There are different types, but they are mainly classified according to the power consumption, the heat transfer medium employed and the contact between the coolant and battery surface; the conventional systems are based on air cooling, liquid cooling, and phase change materials cooling. In general, a BTMS permits to maintain the battery operating temperature in the safe range 15–35 °C [7] and the extent of the cooling depends on the type of the system employed.

State of charge window

A wide literature research was conducted to define the useful state of charge (SoC) window in real application. Several reports are available, with different purposes, amount of data, area and age. One frequent objective is the assessment of the electric vehicle (EV) drivers' attitude towards the recharge phase, especially related to the problem of "range anxiety".

One interesting outcome is that users tend to charge completely their EV battery (i.e. up to a SoC close or equal to 100 %) and to discharge it only partially (the charge phase usually starts from an intermediate SoC level). For instance, Smart et al. [8] performed the assessment of the data collected during the year 2011 from the Nissan LEAF vehicles involved in the U.S. "EV Project". This project was managed by ECOtality North America in the period 2010–2012 with the goal of assessing behavioural and mobility patterns of electric vehicles. For this purpose, a broad network of charging units was installed in eighteen cities belonging to six different U.S. States and vehicle usage data were collected from a fleet of approximately 8300 EVs. According to the 2011 data, the peak of the SoC distribution after a charge is located at SoC $>$ 90 % for the domestic charges, while it is more spread in the range 70 %−100 % if recharges that are performed away from home are considered. Regarding the battery SoC at the start of the charging events, the majority of the recharges begins when the SoC is included in the interval 50 %−60 %. Only few events start at extremely low SoC ($<$20 %).

Corchero et al. [9] analysed a large amount of data related to EVs

usage, collected in different European cities in the period 2011–2013. The authors found that most of the charging processes ends with a fully charged battery and that the average charge behaviour is characterised by an average initial SoC of 60 %. Less than 5 % of the charging events start with SoC < 20 %.

Yang et al. [10] investigated the charging behaviours of fifty battery electric vehicle drivers in Shanghai (China) during the period June 2015 - June 2016. The results of this study are in accordance with the previous report: the charge events start at an intermediate SoC and ends between 90 % and 100 % SoC. Similarly, Zou et al. [11] analysed the behaviour of BEV taxi drivers in Beijing, China, underlining the 40 %−100 % SoC window as the most common utilization region.

Hu et al. [12] employed the cumulative prospect theory, a behavioural science theory that describes the extent of decision-makers' attitudes and preference toward risk, to assess the charging behaviours of EVs users under a mass-market scenario, opportunely modelled. They showed that most of the charging events starts with a SoC belonging to the range 40 %−50 % and that EV drivers do not often decide to begin the recharge at either extremely high or extremely low levels of SoC. In particular, only 2.5 % of charging events starts with SoC 80 % or even higher, and just the 7.5 % falls below the anxiety range (i.e. below 20 % SoC condition).

Lastly, a study by NOW GmbH, a German governmental organization involved in funding programs in the context of sustainable mobility, reports the behaviour of a fleet of BEVs in 2018 and 2019 [13]. They assessed that 59 % of the EV recharges was executed with starting SoC > 70 % and that 86 % of the charging events ended at SoC > 90 %. A summary of this review is provided in Table 1.

Charging C-rate

The review on the most common charging C-rates is here outlined. Tomaszewska et al. [14] states that, in most cases, the maximum charging C-rate in EVs is around 1 C for safety purposes, but in some cases this limit can be extended to 1.5 C. Saxena et al. [15] identified the 0–0.8 C interval as the normal operating range for a lithium-ion battery recharge. Higher C-rates, indeed, can accelerate unsafe mechanisms, such as lithium plating and dendrites formation, hence a value of 1.2 C was estimated by the authors as the maximum limit for the charge processes. In activities that are similar to the present one, Keil et al. [16] performed a C/4 recharge during their driving cycle campaign. On the contrary, Dubarry et al. [17] performed duty cycles consisting of driving cycles as discharge phase and C/5 recharges.

Moreover, taking into account the standard size of Level 2 charging stations and domestic charging available (e.g. 7.4 kW or 11 kW [18, 19]), for a reference BEV battery of 40 kWh as the one considered in this work (whose details are discussed in Section Vehicle model), the corresponding charging C-rate for the battery are in the order of $\sim$ C/10 to C/2. Similarly, for a Level 3 mid-high rate of charge (e.g. 50 kW [18, 19]), the C-rate is close to 1 C.

Table 1
Outcomes of the review on common SoC windows in BEVs.

Source	Publication year	Amount of EVs	Average Starting SoC	Average Ending SoC
Smart et al. [8]	2012	8300	50 %−60 %	> 90 % (private charging) 70 %−100 % (public)
Corchero et al.[9]	2014	689	60 %	> 80 %
Zou et al.[11]	2016	34	40 %	> 90 %
Yang et al. [10]	2018	50	50 %	> 90 %
Hu et al.[12]	2019	-	40 %−50 %	-
NOW-GMBH.DE[13]	2020	219	70 %	> 90 %

Load profile

A driving cycle is a time-speed series that represents a driving pattern, aiming at reproducing a real-world behavior [20]. Among them, standard driving cycles (SDCs) are commonly employed to estimate emission and fuel consumption of vehicles [21,22]. Examples of the most employed SDCs are FTP-75 cycle in US, JC08 in Japan, the New European Driving Cycle (NEDC) and WLTP (World harmonized Light-duty vehicles Test Procedure, detailed in Section WLTP) in Europe.

For instance, A. Tourani et al. [23] in 2014 selected the Common Artemis Driving Cycles (CADC) to investigate the effect of ambient temperature on cell performance, considering this cycle as representative of a real application. The CADC are chassis dynamometer procedures developed within the European Artemis (Assessment and Reliability of Transport Emission Models and Inventory Systems) project, based on statistical analysis of a large database of European real world driving patterns. The cycles include urban, rural road and motorway schedules. In 2017, Keil et al. [16] exploited the American US06 driving cycle to investigate the degradation of lithium-nickel-cobalt-aluminium oxide (NCA) batteries. US06 is an improved version of the FTP-75 to include the highway driving. For this reason, they commented how this standard resembles an aggressive highway driving, with frequent changes between acceleration and deceleration. Thus, it should be considered as a worst-case scenario since EVs are often used in urban traffic conditions, where stop-and-go driving conditions are more frequent, but the load to the battery is usually lower. They performed an extensive and systematic analyses to investigate the role of temperature, depth of discharge (DoD) and regenerative braking, but they restricted their interest to only two indicators, namely capacity fade and resistance increase.

The main shortcoming of standard driving cycles is related to their limited representativeness of the real-world driving conditions [21,24, 25]. As a consequence, there has been a growing concern in the scientific literature about possible misestimations of vehicles' emissions and consumptions performed with the SDCs. In this sense, Diaz et al. [26] stated that the differences between the values obtained using driving cycles and the ones recorded in real-world driving can be up to 60 %. Such differences can be attributed to several factors, such as the traffic conditions of a given area, the drivers' behaviour and the vehicles characteristics (e.g. age, mileage, fuel employed) [20].

In 2019, George Baure and Matthieu Dubarry [17] questioned the use of synthetic driving cycles by comparing the degradation induced by these profiles with real-driving data. In particular, they applied the Federal Urban Driving Schedule (FUDS, a US standard), the dynamic stress test (DST, a simplified version of the FUDS cycle), and the NEDC, since they are the most common ones. First, they discovered that the average current and charge capacity during discharge are important parameters in determining the appropriate synthetic profile, and traffic conditions have a significant impact on cell lifetimes. Moreover, they observed an acceleration of ageing due to the onset of lithium plating. This feature, which has a significant effect on the lifetime prediction, suggests that probing capacity and resistance evolution is not sufficient and a more complete monitoring is required. They suggested the use of metrics that are based on the analysis of degradation modes, e.g. loss of lithium inventory (LLI) and loss of active electrode material (LAM) parameters.

The necessity of a reliable estimation has prompted the development of new and more representative schedules. In this scenario, local driving cycles (LDCs) acquire a great importance. The main feature of this category of driving cycles is that they are developed starting from data directly collected from the vehicles (through GPS devices, for instance) in a specific zone. In this way, a more accurate representation of the driving conditions of the area where data are acquired is obtained. Nevertheless, several researchers work on this topic and, as a consequence, there are various cycles with different characteristics available in the literature. As an example, G. M. S. de Andrade et al. [20]

benchmarked 77 local driving cycles profiles and they identified fluctuations both in the average speed and in the fuel economy, which can affect the results of the degradation tests. On this regard, J. I. Huertas et al. [26] compared three common methods of constructing local driving cycles, namely were the Micro-Trips, the Markov Chains-Monte Carlo and the Fuel-Based. They evaluated if they represent the local driving patterns and their reliability in reproducing the fuel consumption and emissions exhibited by the vehicles in that region. They discovered that Fuel-Based method provides the best performance. This preliminary activity can foster the development of more representative profiles.

Selection of the driving schedule

WLTP

The WLTP (World harmonized Light-duty vehicles Test Procedure) belongs to the family of standardized driving cycles. Developed by the Inland Transport Committee of the United Nations Economic Commission for Europe (UNECE) in collaboration with India and Japan [27], WLTP is the standard procedure applied by all the European Union car manufacturers to determine the emissions and fuel consumption of the traditional and hybrid vehicles and to assess the range of the electric cars. In this activity, this profile is targeted as a representative driving cycle for the experimental campaigns. Its main characteristics are here described.

One WLTP repetition lasts 1800 s, it covers a distance of 23.26 km and it is characterised by an average and maximum speed of 46.5 km h^{-1} and 131.3 km h^{-1}, respectively. Fig. 1 reports the vehicle speed vs time profile of a full repetition. It is commonly divided into four phases. The low-speed phase (first phase) is representative of an urban utilization of the vehicle, hence its average speed (i.e. its average discharge C-rate for the battery) is quite low. On the other hand, this first part of the WLTP cycle is highly dynamic, meaning that it is characterized by many quick accelerations followed by short regenerative brakes (i.e. change between discharge and charge phase for the battery), according to the typical traffic conditions of a city, e.g. roundabouts, traffic lights, stops. Then, the second, third and fourth phases aim at reproducing the suburban, main road and highway driving conditions, respectively. Shifting from one phase to the subsequent one, the average speed progressively increases, while the profile becomes less dynamic. Table 2 the main features of each phase and of the whole WLTP cycle.

IEC 62660-1

The International Electrotechnical Commission (IEC) has developed a dedicated standard schedule, able to accelerate the real aging that vehicles batteries experience: the "Cycle life test" for BEV application of the Normative IEC 62660–1 "Secondary lithium-ion cells for the propulsion of electric road vehicles" [28]. In particular, the IEC 62660–1 cycle is meant to reproduce the degradation of a fully electric vehicle. This profile is considered in this work since it is specifically designed for BEV batteries durability rather than for emissions and fuel consumption estimations. In the following, the term "IEC" is exploited to refer to this normative, for brevity. It is characterized by the following protocol:

- The ambient temperature is set equal to 45 °C.
- Starting from 100 % SoC, the cell is discharged following the dynamic profile A (Fig. 2a). It is a stepped profile, in which each step is characterized by the application of a constant power phase, which is expressed as a percentage of the cell maximum power. The latter, as reported in the normative text, is calculated as follows:

$$P_{max} = X \bullet W \quad (1)$$

where X is the ratio between the required maximum cell power and the energy of the cell and W is the cell electric energy. In the normative text it is stated that a common value for N for commercial batteries for EVs is 3 h^{-1}. W is computed as the product between the nominal capacity C_{nom}

Table 2
Characteristics of the WLTP profile and its phases.

Phase Property	Low	Medium	High	Extra high	Full
Duration [s]	590	433	455	323	1801
Stops duration [s]	145	47	29	6	227
Distance [m]	3095	4756	7162	8254	23,266
Time in stop [%]	24.6 %	10.9 %	6.4 %	1.9 %	-
Maximum velocity [km h−1]	56.5	76.6	97.4	131.3	-
Average velocity [km h−1]	18.9	39.5	56.7	92.0	-
Maximum deceleration [m s − 2]	−1.47	−1.49	−1.49	−1.21	-
Maximum acceleration [m s − 2]	1.47	1.57	1.58	1.03	-

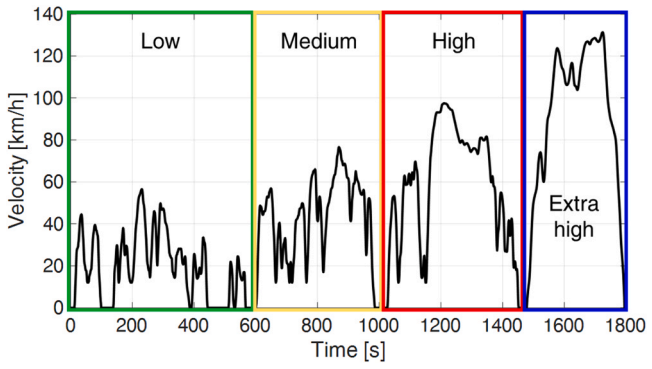

Fig. 1. Velocity vs time profile in a medium SoC condition. Four phases are highlighted.

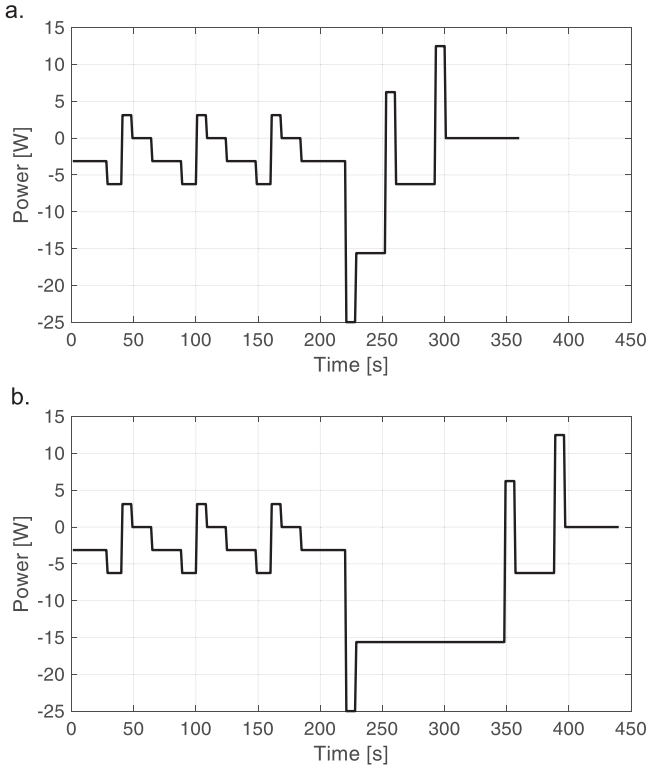

Fig. 2. Power vs time profile for (a) cycle test A and (b) cycle test B of IEC 62660–1.

and the nominal voltage V_{nom}. In this work, the following sign convention holds: negative power values (or C-rate) are associated to the discharge phase of the battery, while positive values refer to the charging phase. In Fig. 2a, it is clear that this profile works mostly in the discharge phase. Profile A is repeated until the cell discharged capacity reaches 50 % of the nominal value.

- The cell is discharged following the dynamic profile B (Fig. 2b) for one repetition. The discharge phase around 300 s refers to the hill climbing period.
- The cell is discharged again with profile A, which is repeated until the discharged capacity equals 80 % of the nominal capacity. When this condition is reached, the cell is brought to the lower voltage limit (i.e. it is fully discharged) through a 1 C constant-current discharge.

Vehicle model

The objective of the vehicle model is to convert a velocity profile into a power profile for the whole battery pack, that can be scaled down to single cells. Depending on the driving phase, the electric power to/from the battery can be computed starting from the vehicle driving power, $P_{driving}$, which can be computed as the total force acting on the vehicle $\boldsymbol{F_{driving}}$, multiplied by the velocity of the car $\boldsymbol{v}$

$$P_{driving} = \boldsymbol{F_{driving}} \bullet \boldsymbol{v} \tag{2}$$

Therefore, it is required to compute the driving force at every time instant. To this aim, all the relevant forces that act on a vehicle have to be listed and a formula for their quantification is needed. A scheme of forces is represented in Fig. 3 and their formulation and description is provided in Table 3. In particular, the following forces are taken into account: rolling resistance (purple arrow in Fig. 3), aerodynamic drag (green), climbing resistance (blue), inertia (red) and weight force (black). This model is inspired by the works of in Keil et al. [29] and in Fiori et al. [30].

For sake of simplicity, as already done by [29] and [30], air speed and road inclination are assumed equal to 0 m s^{-1} and 0 °, respectively. Therefore, the relative velocity of air becomes equal to the vehicle velocity and the climbing resistance is neglected. As a result, the total driving force acting on the vehicle $F_{driving}$ is computed by performing the vector addition of only three forces:

$$F_{driving} = F_r + F_a + F_i \tag{8}$$

In order to compute the battery power, the consumption of the auxiliaries such as lighting, heating or driving assistance must be included. To this aim, a constant power consumption P_{aux} is added in each point of the load profile. Moreover, to convert the mechanical power into electrical, the power flows have to be considered. When the car accelerates, the power flows from the motor to the wheels, whereas, when the vehicle decelerates, the power flows from the wheels to the motor, thanks to the regenerative braking. In the following, power values for the vehicle are considered positive in case of an acceleration phase and negative for deceleration. On the contrary, for battery power values the same convention as in previous section holds. As a result, the power supplied to or extracted from the battery is computed as follows for acceleration and deceleration respectively:

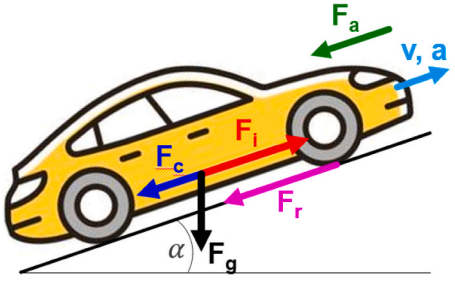

Fig. 3. Scheme of the vehicle model: rolling resistance (F_r in purple arrow, indicating the direction of action), aerodynamic drag (F_a in green), climbing resistance (F_c in blue), acceleration resistance (F_i in red) and weight force (F_g in black). Velocity and acceleration vectors (v, a) show the direction of motion of the car, while α indicates the slope of the road.

Table 3
List and formulation of forces reported in Fig. 3. Symbols description is reported in Table 4.

Symbol	Force	Description	Formulation	
$\boldsymbol{F_r}$	Rolling resistance	friction between tyres and the road	$F_r = (m_v + m_l) * f_r * g * \cos(\alpha)$	3
$\boldsymbol{F_a}$	Aerodynamic drag	force that air opposes to the motion of the vehicle	$F_a = \frac{1}{2} * \rho_{air} * c_w * A * (v + v_{air})^2$	4
$\boldsymbol{F_g}$	Weight force	gravitational force acting on the vehicle	$F_g = (m_v + m_l) * g$	5
$\boldsymbol{F_i}$	Acceleration resistance	inertia acting on the vehicle	$F_i = (m_v + m_l) * a$	6
$\boldsymbol{F_c}$	Climbing resistance	component of the weight force parallel to vehicle velocity	$F_c = (m_v + m_l) * g * \sin(\alpha)$	7

$$P_{battery} = -\left(\frac{P_{driving}}{\eta_{dt} \bullet \eta_m} + P_{aux}\right) \tag{9}$$

$$P_{battery} = -\left(P_{driving} \bullet \eta_{dt} \bullet \eta_m + P_{aux}\right) \tag{10}$$

Where η_{dt} and η_m are drivetrain and electric motor efficiencies, respectively. Hence, the power of the battery pack has to be scaled to cell level dividing $P_{battery}$ by the number of cells N_{cell} inside the battery pack:

$$P_{cell} = \frac{P_{battery}}{N_{cell}} \tag{11}$$

Lastly, power profile can be converted into cell current I_{cell}, as

$$I_{cell} = \frac{P_{cell}}{V_{cell}} \tag{12}$$

where V_{cell} is the nominal voltage of the cell, as in Keil et al. [29]. Since cell voltage varies with SoC and C-rate, this approximation under/-overestimates the real voltage value, especially at extreme values of these variables. The conversion from power to current is required by the experimental equipment, but it is also important to estimate the state of charge during the cycle.

Model validation

To validate the model, it is employed to simulate the behaviour of a real BEV, whose data have been collected and made freely available by the Argonne National Lab. The vehicle is a BMW i3 2014, tested on roller bench with an Urban Dynamometer Driving Schedule (UDDS) and an US06 driving cycles [31]. The input parameters of the model are listed in Table 4, both for the vehicle and the battery pack. The battery pack consists of 96 series-connected cells of 60Ah each. Nominal conditions refer to 50 % SoC, namely 3.7 V and 355 V for each single cell and the whole pack, respectively.

Starting from the speed-time profile of the driving cycles, i.e. UDDS and US06, the power-time profile is derived by means of the equations reported in Section Vehicle model. Analysing the power consumption of the experimental data when the car is at idle, the auxiliary consumption P_{aux} is estimated equal to 160 W. From the power profile it is possible to derive the corresponding current profile. Velocity, mechanical power and battery pack current profiles are represented in Figure S.1 of the

Table 4
BMW i3 2014 parameters adopted for vehicle model validation with characteristics of the battery pack, obtained from [31].

Symbol	Parameter	Value
m_l	Load mass [kg]	1300
m_v	Vehicle mass [kg]	150
A_a	Vehicle cross-sectional area [m^2]	2.38
η_{dt}	Drivetrain efficiency [-]	0.95
η_m	Electric motor efficiency [-]	0.91
f_r	Rolling resistance coefficient [-]	0.012
ρ_{air}	Air density [kg m−3]	1.2
c_w	Drag coefficient [-]	0.29
$\boldsymbol{v_{air}}$	Air velocity [m s − 1]	0
g	Gravitational acceleration [m s − 2]	9.81
α	Inclination of the road [°]	0
P_{aux}	Auxiliaries' consumption [W]	160
N_{cell}	Number of cells in the battery pack [-]	96
	Battery pack nominal voltage [V]	355
	Battery pack nominal energy [kWh]	18.8
	Number of cells [-]	96
	Cells configuration	96S1P
	Cell nominal voltage [V]	3.7
	Cell nominal capacity [Ah]	60

Supplementary Materials.

The validation is performed by comparing the C-rate profile derived by the model to the corresponding profile measured experimentally. Fig. 4 reports the experimental C-rate against the model C-rate: when a point is near to the bisector (orange line) or it even overlaps, it means that the model C-rate is similar to the experimental one. Differently, if a point is above the bisector it means that the model overestimates the C-rate and if below it is the other way round. All the plotted points are near the bisector in the entire interval of interest, with a mean error equal to 0.045 h^{-1}. The distribution exceeds both above and below the target line, without offsets, confirming the meaningfulness of the approach. Hence the model estimations of the C-rate are considered realistic and model validation satisfactory.

Conversion of WLTP into power profile

The vehicle model is applied to convert the WLTP profile into a power profile and scale it to single cell for its experimental application. Therefore, a typical, generic mid-size EV is identified as reference, aiming to generalize the investigation without referring to any specific commercial case. The battery pack is hence assumed as if it was constituted by single cells specified in Section 4. Analogously, an automotive-like reference average condition is assumed for auxiliaries' power consumption such as HVAC, consistently with [32]. The parameters are summarized in Table 5. The resulting cell C-rate vs time profile is reported in Fig. 5, associated to a medium SoC condition, namely assuming 3.7 V and 3.85 V as average voltage for discharge and charge phases, respectively.

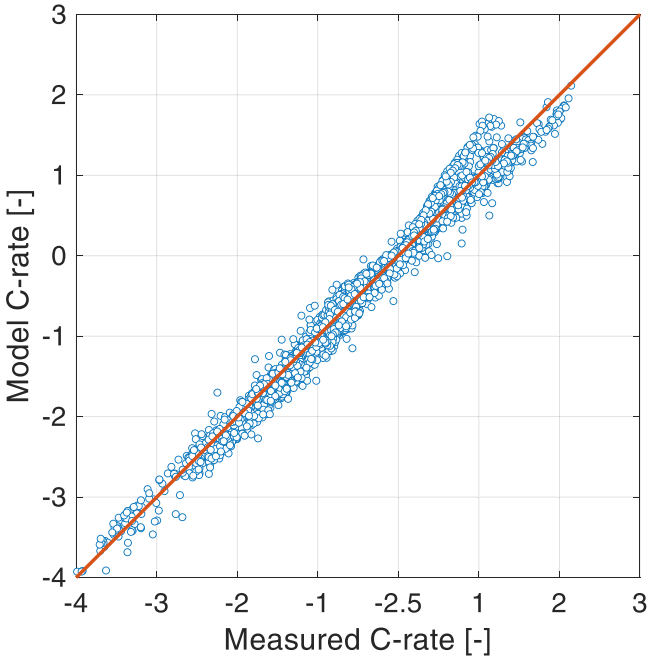

Fig. 4. Model cell C-rate plotted against experimental cell C-rate during UDDS+US06 profile.

Consistency of WLTP with respect to a real application

The local driving cycle WPG02 [33] has been constructed on the basis of GPS data recorded from a fleet of 76 EVs over a period of one year (May 2008 - June 2009) in the city of Winnipeg, Canada. The volunteer participants were selected from different income brackets, education levels, genders and districts of the city, in order to create a statistical population that best represented the drivers' behaviours in the area. Taking into account intrinsic differences in vehicle usage profiles during weekdays and weekends, two distinct speed-time profiles have been developed: during weekends, the traffic is generally dampened, hence the cycle is less dynamic and the idle intervals are definitely shorter. Hence, the average speed of the weekend cycle is higher than that of the weekdays.

The weekdays WPG02 has been used to validate the choice of the WLTP as reference cycle for the experimental campaign conducted in this work. To do that, its speed-time profile is converted into C-rate vs time profile through the application of the procedure described in Section 3.3. Profiles are showed in Figure S.2 of the Supplementary Materials. In Table 6 the main features of the speed and current profiles of the weekdays WPG02 and WLTP have been compared.

In order to perform a fair and reliable comparison, the time dependent characteristics associated to WLTP have been re-scaled, since the duration of the two profiles is different (1800 s vs 3483 s). Moreover, WLTP has been curtailed for the extra high-speed phase, because WPG02 does not account for highway utilization of the electric vehicles. This is consistent to the period in which WPG02 has been built, when EVs were rarely used out from the cities. Comparing the information in Table 6 for the two profiles, it is possible to observe that the parameters of the two cycles are highly comparable, especially the number of regenerative braking events, the average C-rate (i.e. the average speed), the maximum C-rate in charge and discharge and the ΔSoC. Therefore, it is proved that WLTP is representative for a real utilization of an electric vehicle and it is possible to apply the WLTP profile in reproducing close-

Table 5
Vehicle model parameters.

Parameter	Value
Vehicle mass [kg]	1300
Load mass [kg]	150
Vehicle cross-sectional area [m^2]	2.38
Drivetrain efficiency [-]	0.95
Electric motor efficiency [-]	0.91
Rolling resistance coefficient [-]	0.012
Air density [kg m−3]	1.225
Drag coefficient [-]	0.29
Air velocity [m s − 1]	0
Gravitational acceleration [m s − 2]	9.81
Inclination of the road [°]	0
Auxiliaries consumption [kW]	1
Battery pack nominal energy [kWh]	40
Battery pack nominal voltage [V]	355
Number of cells in the battery pack [-]	4800
Cells electrical configuration [-]	96S50P
Cell nominal voltage [V]	3.7
Cell nominal capacity [Ah]	2.25

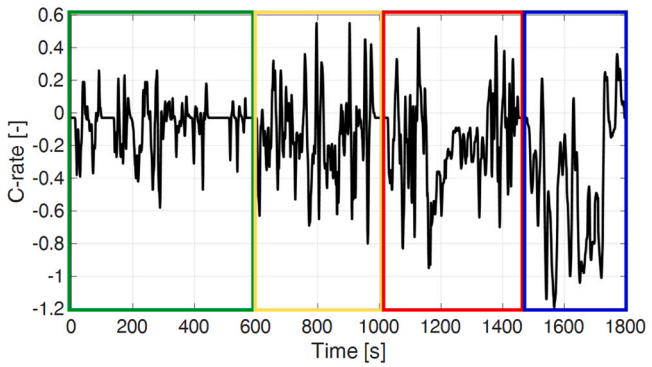

Fig. 5. C-rate vs time profile in a medium SoC condition. Four phases are highlighted.

Table 6
Comparison between the rescaled WLTP without phase 4 (Extra High Speed) and the Weekdays WPG02.

Parameters	WLTP (rescaled, no Phase 4)	Weekdays WPG02
Number or regenerative braking events	238	275
Average Speed [km h−1]	36.6	32.6
Maximum Speed [km h−1]	97.4	99.6
Average C-rate [-]	−0.12	−0.11
Average C-rate (discharge only) [-]	−0.187	−0.174
Average C-rate (charge only) [-]	0.130	−0.141
Maximum C-rate (discharge only) [-]	−0.946	−0.980
Maximum C-rate (charge only) [-]	0.552	0.889
Charge exchange (discharge only) [mAh]	286.6	303.9
Charge exchange (charge only) [mAh]	53.1	61.3
Charge exchange (net) [mAh]	233.5	242.5
State of charge variation [%]	10.4	10.8
Range [km]	304	293

to-real-world profiles for EVs.

Comparison between WLTP and IEC profiles

The IEC 62660–1 standard has been selected as the second profile in the experimental campaign: being a normed cycle, it provides reliability and universality to the results. In Table 7, the main parameters of the complete profile are compared with those of a sequence of WLTP cycles, which is repeated several times in order to bring the cell from 100 % to 0 % SoC. It is possible to observe that, for the standard, the average and maximum C-rates both in charge and discharge phases are higher, hence its adoption in the experimental campaign permits to investigate the effect of high currents application on the cells degradation. On the other hand, it is less dynamic compared to WLTP, being a stepped profile without frequent acceleration or regenerative brakings.

Moreover, in order to investigate the effect of the characteristics of the profile on battery degradation, e.g. highest charging C-rate or number of brakings, a third cycle named “WLTP High Speed”, composed by the last two phases of WLTP (High-Speed and Extra High-Speed), is selected for the experimental campaign. Its C-rate vs time profile is depicted in Fig. 6. WLTP High Speed represents a sort of trade-off between IEC 62660–1 and WLTP profiles in terms of amplitude of the currents and cycle dynamics, as in Table 8. All the values reported in the table are referred to a medium SoC condition.

Table 7
Comparison between the characteristics of IEC 62660–1 and WLTP profiles.

Parameter	IEC 62660-1	WLTP
Average C-rate [-]	−0.480	−0.178
Average discharge C-rate [-]	−0.875	−0.258
Average charge C-rate [-]	0.173	0.136
Max discharge C-rate [-]	−3.978	−1.407
Max charge C-rate [-]	1.441	0.579

Methodology

Samples and testbench description

The characteristics of the experimental samples are listed in Table 9. They are commercially available high-energy cells, with blended positive electrode made of lithium-nickel-cobalt-manganese-oxide (NMC) and lithium-manganese oxide (LMO), considered as representative of a BEV sample. All samples have been tested before the start of the campaign, showing limited differences of performance. No information is available regarding electrolyte and binder compositions.

The testing station was described in [2]. It is a custom solution, including a single power supply with two five-channels electronic load, resulting into eight independent testing channels, able to perform EIS. All cells are located in a Binder MKF 720 Eucar 6 climatic chamber to undergo tests under controlled temperature and humidity. Test temperature always refers to the setpoint of the climatic chamber. One type K thermocouple is attached on the surface of the samples to monitor its temperature evolution.

Test matrix

As a result of the literature review discussed in Section 2 to assess the conditions of real ageing, the following cycles were executed, as listed in Table 10. Overall, these reasonings were applied:

- *Temperature*: when possible, the same cycle is performed at two different temperature levels, since temperature is known to be a relevant factor in determining degradation. While 25 °C is an average temperature of the application, the 45 °C temperature enables to induce a temperature-related degradation along the driving phase, to account for the parking phases of a car that are not included in the driving profile. Indeed, a car is left parked (rest phase of a battery) for more than 90 % of its total lifetime on average, thus their role must be investigated. The 45 °C is also applied in the calendar ageing campaign, thus its role can be subtracted from the cycles at high temperature, to split between cycle-related and calendar-related degradation. Lastly, this choice is prescribed by the IEC 62660-1 standard.
- *SoC Window*: the most common state of charge window lies within 100 % and 50 % SoC, which is selected as benchmark case (lines 2 and 7 in Table 10). Other combinations of SoC windows enables the

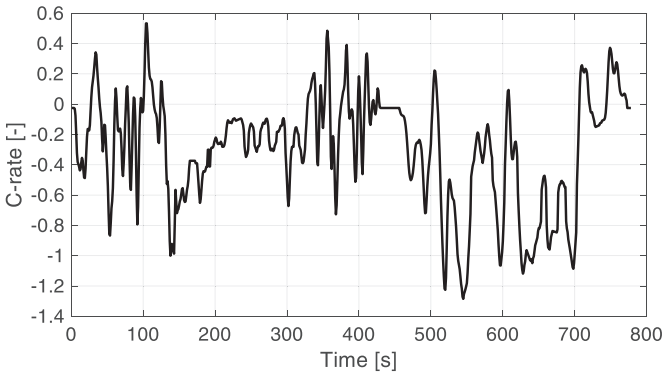

Fig. 6. C-rate vs time profile of the WLTP High Speed.

Table 8
Comparison among WLTP, WLTP High Speed and IEC 62660–1 profiles A and B.

Parameters	WLTP	IEC 62660-1 A	IEC 62660-1 B	WLTP High Speed
Average C-rate [-]	−0.175	−0.37	−0.69	−0.29
Average discharge C-rate [-]	−0.25	−0.76	−1.11	−0.38
Max discharge C-rate [-]	−1.193	−3.00	−3.00	−1.19
Average charge C-rate [-]	0.134	0.68	0.68	0.16
Max charge C-rate [-]	0.552	1.50	1.50	0.52
Duration [s]	1800	360	456	778
ΔC [mAh]	197	84.4	189.6	139.4
ΔSoC [%]	8.74	3.75	8.43	6.19

Table 9
Characteristics of the experimental samples [34].

Property	Value
Manufacturer	SONY
Model	US18650V3
Nominal capacity	2.25 Ah
Voltage cut-offs	2.5 V−4.2 V
Electrode materials	Graphite/NMC+LMO
Continuous max charge C-rate	1 C

investigation of this stressor by comparison. Indeed, the 50 %−0 % SoC cycle (line 10) investigate the same load cycle, same recharge current and depth of discharge, but applied on a different SoC window. The 100 %−75 % and 75 %−50 % and cycles cover portion of the same window, but with a little DoD. Moreover, the full SoC window is also applied, to allow possible comparison with the existing scientific literature, where deep discharge cycles are common. Moreover, this choice is prescribed by the IEC 62660-1 standard.

- *Load Profile*: the WLTP is selected after the validation over local driving cycles. IEC 62660-1 is also performed to investigate the effect of the load profile. Lastly, as an intermediate case, the WLTP High-Speed is also applied in one case.
- *Recharge C-rate*: C/3 is chosen as benchmark charging C-rate, but C/6 and 1 C are performed, too. C/6 is closer to a domestic charging rate, while 1C is a closer to fast charge. Moreover, as reported in Tables 9, 1C is considered as maximum C-rate since it is the maximum continuous value recommended by the manufacturer.

At the beginning, all the cells are pristine, with a difference in capacity within 1 %. After a while, the campaigns are interrupted to evaluate the residual performances of the cells. Two cells underwent the same profile, for repeatability purposes.

100 % SoC is achieved after a CC charge at C/10 until 4.2 V with constant voltage hold until current drops below 0.05 A. State of charge is always defined with reference to nominal conditions (e.g. 75 % SoC corresponds to discharging by 25 % of the nominal capacity, starting from 100 % SoC).

Characterization procedure

Characterization tests are performed along the campaign to map the evolution of degradation effects. In particular, only the data regarding C/10 full discharges at 25 °C are here investigated. C/10 and 25 °C are identified as a suitable condition to mimic quasi-equilibrium conditions in a preliminary activity, comparing different charge and discharge processes at several temperature and C-rates conditions. This choice has been already performed by other research groups in the literature [35].

Equilibrium model

An equilibrium model is applied to identify loss of lithium inventory and loss of active electrodes material by reproducing the differential voltage curve of the C/10 and 25 °C discharge. It is freely available here. The model is 0D. It includes the open-circuit potential (OCP) curves of the electrodes, measured experimentally in coin-cell setup with lithium counter electrode (half-cell). Cell voltage is estimated as the difference between OCP values of positive and negative electrode, summed to a lumped resistance that considers ohmic and kinetic voltage drops. This resistance is SoC-invariant and it is estimated experimentally.

For the fresh cell, stoichiometric operating boundaries of the electrodes are directly estimated with half-cell experimental testing. For an aged state, a non-linear solver is exploited to match the OCP curves at battery 100 % SoC, by imposing the maximum cut-off voltage while ensuring the charge balance between the electrodes. After the identification of the 100 % SoC condition, the discharge is simulated at the desired constant C-rate, until the voltage drops below the lowest voltage cut-off. The C/10 25 °C discharge of the fresh cell is described in Section

Table 10
List of cycles with corresponding operating conditions. “EFC” for equivalent full cycle.

#	Label	Temperature [°C]	Load profile	Maximum SoC [%]	Minimum SoC [%]	Charging C-rate [-]	Total time [day]	Total charge [EFC]	#
1	WLTP 100 %−0 % 45 °C	45	WLTP	100 %	0 %	C/3	99	290	1
2	WLTP 100 %−50 % 45 °C	45	WLTP	100 %	50 %	C/3	148	395	2
3	WLTP High-Speed	45	WLTP High-Speed	100 %	0 %	C/3	148	500	3
4	IEC C/3 45 °C	45	IEC 62660−1	100 %	0 %	C/3	121	530	4
5	IEC C/6 45 °C	45	IEC 62660−1	100 %	0 %	C/6	109	357	5
6	WLTP 100 %−0 % 25 °C	25	WLTP	100 %	0 %	C/3	162	448	6
7	WLTP 100 %−50 % 25 °C	25	WLTP	100 %	50 %	C/3	161	419	7
8	WLTP 100 %−75 % 25 °C	25	WLTP	100 %	75 %	C/3	159	382	8
9	WLTP 75 %−50 % 25 °C	25	WLTP	75 %	50 %	C/3	114	301	9
10	WLTP 50 %−0 % 25 °C	25	WLTP	50 %	0 %	C/3	92	282	10
11	IEC C/3 25 °C	25	IEC 62660−1	100 %	0 %	C/3	109	455	11
12	IEC C/6 25 °C	25	IEC 62660−1	100 %	0 %	C/6	160	458	12
13	IEC 1 C 25 °C	25	IEC 62660−1	100 %	0 %	1 C	92	449	13

S3 of the Supplementary Materials.

LLI accounts for all the mechanisms that induce a decrease of cyclable lithium, without affecting the structure of the electrodes. On the contrary, LAM parameters (LAMp and LAMn for positive and negative electrode, respectively) induce a reduction of active sites, available for lithium (de-)intercalation, without affecting the total amount of cyclable lithium (purely deithiated LAMs). Under the assumption of quasi-equilibrium, all the other classes of losses like kinetic, resistive and mass transport-related are neglected for the purpose of this C/10 discharge. Parameters are identified by means of a Particle Swarm Optimisation (PSO) algorithm, providing the best fit of the experimental data by matching the OCP curves of the electrodes.

Parameters value is reported as an optimal value and a confidence interval. The first refers to the best solution that the algorithm has found in the parameter identification process, whereas the second refers to a range of values that produce a similar result on the protocol tests. The difference due to this change of parameter value is so little that, other than slight numerical variations, it is not possible to state which solution is better reproducing the experimental data. It is meaningful to trace this interval, in order to assess whether the variation of one parameter is relevant or not. For more information regarding model structure, parameter identification and interval determination, the reader is referred to [3].

Evolution of LAMp and LAMn of two cells has been also estimated with a charge-based method, as reported in Section S4 of the Supplementary Materials, providing a consistent result.

Results

Capacity loss

The evolution of capacity loss for all the tested samples is reported in Fig. 7. To improve the readability, the plot is split into two subfigures: cycles at 25 °C and 45 °C in subfigures a and b, respectively. Capacity loss Q_{loss} is computed as

$$Q_{loss} = \frac{Q_{BOL} - Q_{act}}{Q_{nom}} \tag{13}$$

where Q_{BOL}, Q_{act} and Q_{nom} are the measured capacity at begin of life (BOL), the one at a certain ageing state and the nominal capacity from the datasheet, respectively.

The first difference is associated with the ambient temperature. Cycling at 45 °C induces a faster degradation. J. Stadler et al. [36] observed very similar trends in their investigation of NMC622 degradation under dynamic cycling, linking high temperature with an improved kinetics of side reactions. Second, comparing the various shades of blue, the effect of the recharge current seems limited, as in [36]. They are very similar in Fig. 7a, while the difference in Fig. 7b vanishes if the two cycles are plotted against operating time instead of charge. This fact suggests a role of calendar ageing, as proposed also in [36].

Comparing the shades of orange in Fig. 7a, the effect of SoC and DoD is highlighted. Lastly, Fig. 7b shows the green curve related to the WLTP High-Speed profile, which is very similar to the IEC profile with same charging current, thus its effect seems limited. Similarly, comparing WLTP and IEC no significant differences emerge at both temperatures.

For a first, more quantitative overview of the capacity loss as a function of the investigated stressors, a linear fit is performed for all the cells and the coefficients are listed in Table 11. A square-root fit is avoided, since the linear fit shows always a satisfactory R^2 value. A second fitting approach involves a linear fit with the additional degree of freedom of the intercept. It provides even higher R^2, but no great variations occur to the linear coefficients. They slightly decrease, since the large growth at the beginning is included in the constant term. Values of

Table 11
Fitting of capacity loss trends for the driving cycle campaign. "Coeff" for coefficient, "Interc" refers to the intercept with the y-axis. Coefficients in EFC^{-1}.

#	Cell	Linear fit		Linear (neglect the first point)		
		Coeff	R^2	Coeff	Interc	R^2
1	IEC 25 °C 1 C	0.0245	0.942	0.0238	0.545	0.973
2	IEC 25 °C C/3	0.0234	0.853	0.0210	0.994	0.934
3	IEC 25 °C C/6	0.0217	0.991	0.0214	0.170	0.993
4	WLTP 25 °C C/3 100 −0 %	0.0221	0.990	0.0218	0.177	0.994
5	WLTP 25 °C C/3 100 −50 %	0.0290	0.906	0.0264	0.952	0.968
6	WLTP 25 °C C/3 100 −75 %	0.0194	0.917	0.0170	0.627	0.959
7	WLTP 25 °C C/3 75 −50 %	0.0182	0.971	0.0175	0.264	0.982
8	WLTP 25 °C C/3 50 −0 %	0.0168	0.942	0.0183	−0.197	0.968
9	IEC 45 °C C/3	0.0340	0.983	0.0319	0.789	0.991
10	IEC 45 °C C/6	0.0365	0.898	0.0311	1.655	0.947
11	WLTP 45 °C C/3 100 −0 %	0.0363	0.914	0.0315	1.500	0.947
12	WLTP 45 °C C/3 100 −50 %	0.0477	0.831	0.0416	1.928	0.901
13	WLTP High Speed 45 °C C/3	0.0350	0.976	0.0336	0.732	0.992

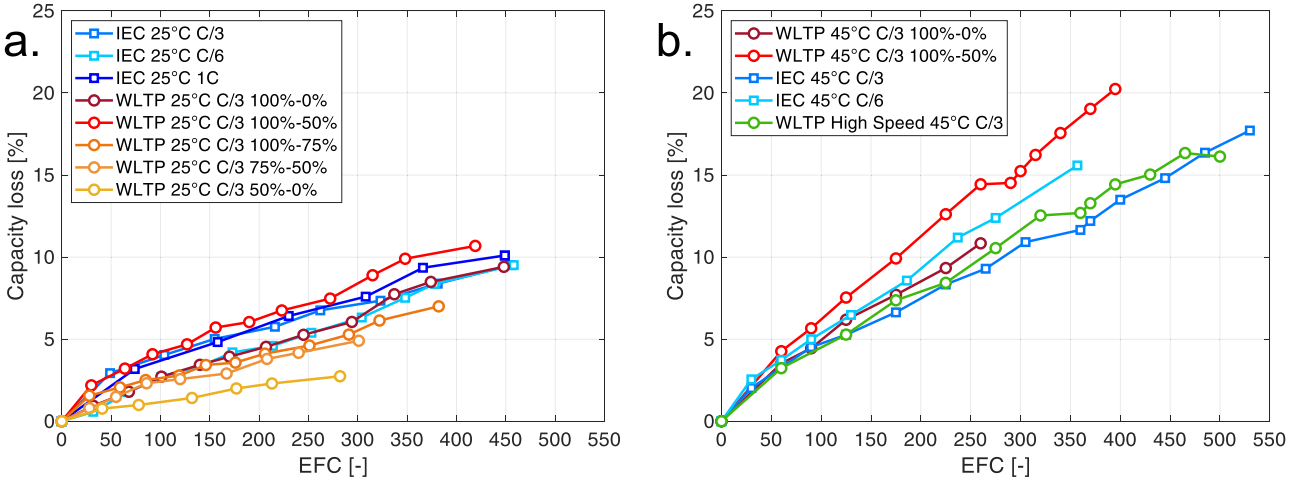

Fig. 7. Capacity loss evolution vs EFC of all the driving cycle cells: a) cycles at 25 °C and b) cycles at 45 °C.

the coefficients support the early observations regarding Fig. 7. More in depth, comparing the coefficients of the cycles that have a counterpart at both temperatures (e.g. lines 2 and 9 in Table 11, IEC profile at 25 °C and 45 °C), a ratio around 2/3 is estimated. It means that an increase of 20 °C is equivalent to a 50 % higher capacity loss over charge basis. Furthermore, this table stresses the similarity between different load profiles (e.g. lines 9, 11 and 13) and the role of the state of charge window (for instance, lines 5 vs 8 and 11 vs 12).

Thermodynamic losses

Evolution of DV The IEC cycle performed at 25 °C with C/3 recharge C-rate is selected as example for the in-depth analysis. First, the q-OCP analysis of the differential voltage (DV) is reported. The nomenclature of the main peaks and valleys is detailed in Figure S.3 of the Supplementary Materials (showing positions of positive and negative electrodes peaks). From left to right of Fig. 8b, peak F1 and F2 are clearly identifiable, attributed to the phase transitions of LMO (P1 and P2 in Figure S.3) superimposed to that of graphite (N1 in Figure S.3). Then, at low SoC the third peak F3 is noticeable, due to graphite following three short phase transitions (N2 in Figure S.3) ending with a steep voltage increase at an almost fully delithiated state, leading cell voltage down to the low voltage limit.

Experimental discharge and DV at increasing degradation stages are reported in dashed lines in Fig. 8a and b, respectively. Capacity loss is evident, as the leften movement of the plateau at 3.65 V. In the DV (Fig. 8b), the low-SoC peak F3 shifts towards the left progressively. Moreover, it looks less and less defined as the campaign proceeds, losing the information related to the smaller phase transitions of graphite. This fact is correlated to a C-rate effect: as the cell ages, the assumption of quasi-equilibrium is challenged. Additional tests at the end of the campaign verified that the only effect involves the low SoC peak, which becomes blurred. Figure S.6 of the Supplementary Materials deals with this topic. The cost function for the identification of thermodynamic parameters have been improved to take this effect into account, as explained in [3].

Furthermore, high SoC peaks F1 and F2 move, too. The relative distance between F2 and F3 seems decreasing over time. The simulations of the equilibrium model are depicted in full lines. First, the model follows the trend of capacity loss. On the DV plot, the evolutions of the peak are well reproduced, especially that of F1. As already mentioned, the magnitude of the peaks, especially F3, is not properly reproduced due to the too high C-rate for the assumption of quasi-equilibrium. Overall, this result is considered accurate.

Thermodynamic parameters evolution

The corresponding thermodynamic parameters values are reported in Fig. 9. The trends are clear with little confidence bands, apart from the last stages because some peculiar features of the DV become blurred. Loss of active electrode material (LAM) of the negative electrode (LAMn) has a steep trend at the beginning (until 50 EFC) followed by a stabilization. LAMp is linear over time, while LLI has an initial growth followed by a linear trend, consistent to that of the capacity loss.

The evolution of LAMn is shared by all the cells and it is associated with a stabilization of the material. Similar trends were already observed in different campaigns on the same cell type, uncorrelated with the operating conditions [3,4]. The average value for 25 °C cycled cells is around 8 % for cycles at 25 °C, while a value close to 10 % is identified for 45 °C ones, as in the calendar ageing campaign in [4].

LAMp can be related to transition metal dissolution, cathode electrolyte interphase (CEI) growth and cation mixing, but also to particle cracking [37–40]. As a matter of fact, charge/discharge cycles are known to induce volume variations of the electrode [37,40]. This mechanism, particularly relevant for large DoD levels, can induce cracking of the particles, which may become inactive or develop weaker connection with the conductive matrix. These possibilities are further evaluated in the following analyses.

Lastly, LLI can be associated with side reactions with the electrolyte (leading to well-known SEI growth) and with lithiated LAMs [41–44]. However, it is hard to distinguish the share of these two contributions, since it is impossible to define the lithiation level in the electrodes when they lose active sites (leading to LAM). Nevertheless, it is reasonable to assume a linear growth over cycles of the component related to SEI growth and at least 40 % of the total lithium loss can be correlated to the sum of lithiated LAMs.

Effect of the operating conditions

Cycles are compared in small groups, where only one operating condition is different, to highlight its effect.

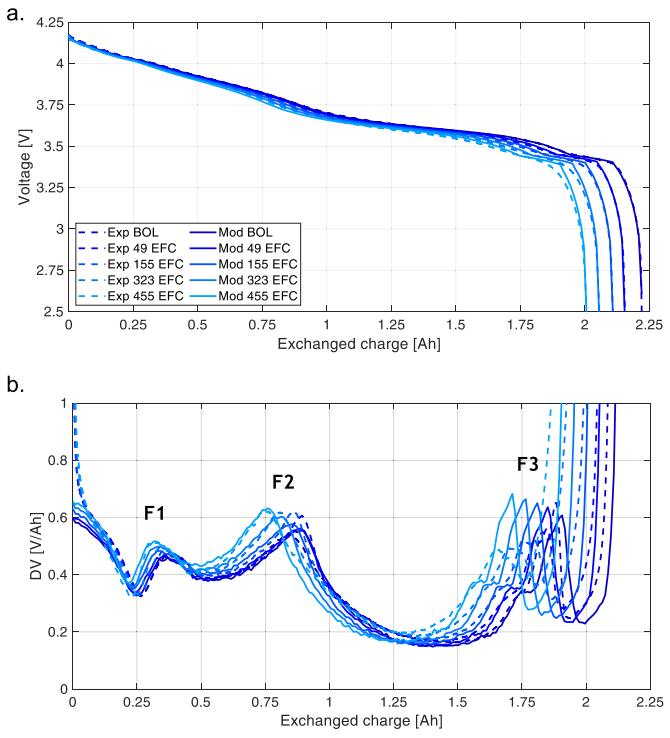

Fig. 8. Experimental (dashed lines) and modelled (full lines) a) discharge curve and b) differential voltage of the cell cycled at 25 °C with IEC profile, at various check-ups. Nomenclature of the peaks in subfigure b) is described in the text.

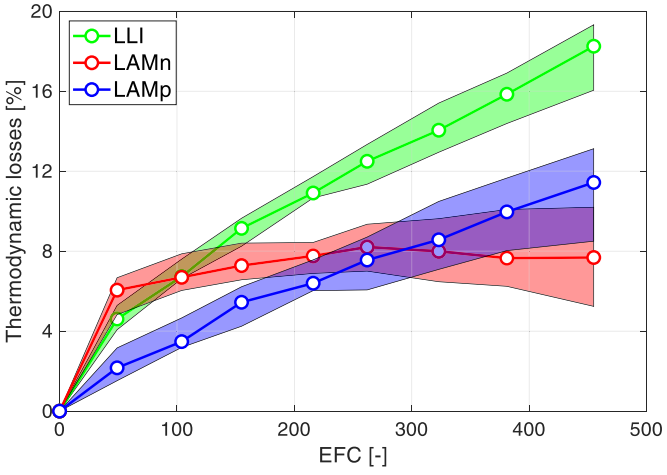

Fig. 9. Trend of the thermodynamic parameters for the cell cycled at 25 °C with IEC profile.

Recharge C-rate

The recharge current is investigated by comparing the parameters value of the cycles that share all the operating conditions but the recharge C-rate, namely.

- IEC cycle at 25 °C, between 100 % and 0 % SoC, with 1 C recharge C-rate
- IEC cycle at 25 °C, between 100 % and 0 % SoC, with C/3 recharge C-rate

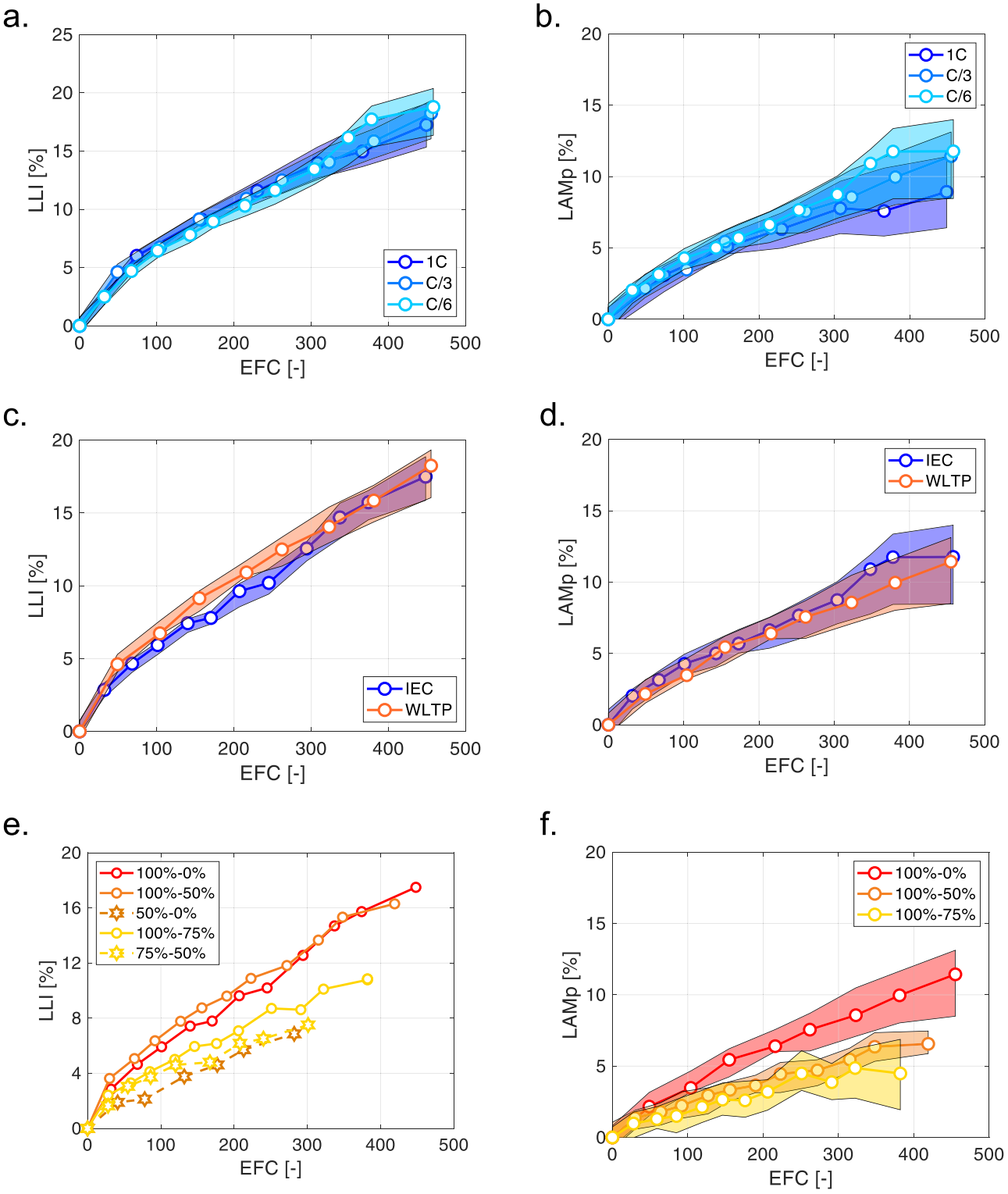

Fig. 10. Comparison between the evolution of thermodynamic parameters for some cycles with uncertainty bands. a) LLI and b) LAMp for IEC 25 °C cycles, highlighting the effect of recharge C-rate. c) LLI and d) LAMp of WLTP and IEC 25 °C cycles, highlighting the effect of the load profile. e) LLI and f) LAMp and d) LLI of some WLTP 25 °C cycles, highlighting the effect of the state of charge window. In e) confidence bands are avoided to improve the readability. Details of the important operating conditions are reported in legends.

- IEC cycle at 25 °C, between 100 % and 0 % SoC, with C/6 recharge C-rate.

The capacity loss trend is almost equal for all the investigated conditions. Similarly, LLI values almost overlap if estimated at an equal amount of charge throughput. Its chart is reported in Fig. 10a. LAMp evolution is similar for all the cells (Fig. 10b), too. The confidence intervals of LAMp overlap for the three cases at the beginning and remain close at high EFC values. Moreover, at the end the interval widens, due to blurred features of the DV in these conditions (Section Thermodynamic losses). Despite a factor of six between the lowest and the largest C-rates, no significant difference is recorded. Considering that the cycles have worked in the same SoC window, it is reasonable to assume a similar contribution of lithiated LAMp to the overall lithium inventory loss.

Hence, the effect of the recharge C-rate is negligible in the investigated conditions of temperature (25 °C and 45 °C, not shown for brevity) and C-rates (C/6, C/3 and 1 C). This result, though unexpected, is consistent with the specifications of this cell type. As a matter of fact, the suggested maximum charge C-rate is 1 C in the temperature range of interest. It is noteworthy how the degradation, considering various aspects of the battery operation, of all cycles proceeds analogously and at the same pace on charge basis. Moreover, at 45 °C the timespan becomes important, suggesting the occurrence of calendar ageing (see capacity loss trend Section Capacity loss).

Load profile

WLTP and IEC cycles at 25 °C with same charge C-rate and SoC window are compared to visualize the effect of the load profile. The trend of capacity loss showed a similar trend with EFC for the two profiles, both at 25 °C and 45 °C. LLI for both cells follows the trend of capacity loss (Fig. 10c), showing limited differences. Interestingly, LAMp shares a very similar growth, too, as reported in Fig. 10d. As a consequence, the thermodynamic analysis supports a limited effect of this variable, despite the differences (Section Comparison between WLTP and IEC profiles).

State of charge window

Different WLTP cycles at 25 °C are compared to identify the role of SoC and DoD. Due to their inherent interdependence, they are analysed together.

The trend of LLI (Fig. 10e) is complex. Cycles sweep different SoC intervals: 100 %−0 % (red curve, circle market), 100 %−50 % (orange, circle), 100 %−75 % (yellow, circle), 50 %−0 % (orange, star marker) and 75 %−50 % (yellow, star). Confidence bands are avoided for readability. It is worth highlighting that all the considered cycles operate at different average SoC. There is an interplay between SoC and DoD. At fixed DoD, high LLI is assigned to high SoC of cycling. On the other hand, high LLI is assigned to high DoD, as in [45], at a prescribed SoC. The difference between 100 %−50 % and 50 %−0 % SoC is very strong. Low SoC is a favourable condition with respect to ageing, as already stated in literature [45]. Between 100–75 % and 75–50 % SoC the differences are little. Overall, large LLI at high SoC are consistent with SEI growth. The similarity between 100 %−50 % and 100 %−0 % cycles can be associated with the trend of LAMp (Fig. 10f): if LAMp is significantly lithiated, it can compensate for the time that the 100 %−0 % cycle spends at low SoC.

Indeed, Fig. 10f shows the evolution of LAMp with uncertainty bands for the cycles that sweep the 100 %−0 % (red curve and area), 100 %−50 % (orange) and 100 %−75 % (yellow) SoC intervals. It looks like the larger the DoD, the larger the LAMp. Moreover, as already discussed, LAMp trend is independent on the recharge current and the load profile. This difference is meaningful and supports the occurrence of a mechanical effect: large depth of discharge induces large volume variations in the electrodes, thus they are more susceptible to particle cracking [40]. It is noteworthy that this difference does not exist at 45 °C between 100 %−0 % and 100 %−50 % cycles (not shown for brevity). It might be related to improved mechanical properties of the material thanks to a higher temperature.

Temperature

Lastly, the role of ambient temperature is here discussed. The trend of capacity loss showed a strong effect of temperature, with 45 °C-cycled cells exhibiting a faster capacity loss rate by ~50 % with respect to the same cycle at 25 °C. Fig. 11a shows the comparison of capacity loss trend over time for three cells:

- IEC cycle at 25 °C C/3 (red curve)
- Calendar aged cell at 45 °C and 50 % SoC (yellow), investigated in [4]
- IEC cycle at 45 °C C/3 (black)
- The sum of the first two (orange)

It is worth reminding that the comparison between the two cycles would not change if the data were plotted against EFC.

Interestingly, the superposition of effects holds true. As a matter of fact, there is quite a good agreement between black and orange curves. It suggests the possible distinction between usage-related and calendar-related losses and that the two effects linearly sum up. More clearly, the capacity loss of a high temperature cycle is suitably reproduced by the capacity loss of the same cycle, carried out at 25 °C, and that of the calendar aged cell that is stored at the intermediate SoC of the interval that is spanned by cycle (e.g. in this case 50 %, since both cycles operate in the 100 %−0 % SoC range).

This result is already present in the scientific literature [45,46], though it has been questioned [47]. The unexpected and novel result lies in the application of this method on thermodynamic parameters. Fig. 11b-c-d shows the same analysis, comparing the evolution of LLI, LAMp and LAMn, respectively. LLI and LAMp of the high-temperature cycle are reliably represented by the superposition of the low-temperature cycle and the high-temperature calendar ageing at the intermediate SoC, considering the same time span. LAMn is reported for the sake of completeness but, as already mentioned, its trend is the same for all the tested cells, thus it can be assumed that the same stabilization phenomenon is occurring in all the cells, at the same pace.

Similar results are achieved for all the tested cycles conditions that have a counterpart at both temperatures and they support a universality of the principle, at least in the investigated temperature range. They are reported in Figure S.7, S.8 and S.9 of the Supplementary Materials. This analysis is of particular interest for prediction methods and for an improved design of experiments, since it enables to avoid some testing conditions.

In conclusion, there is a strong effect of temperature. Cycling seems to induce a fast capacity loss which can be associated with SEI growth, but also a significant deterioration of the positive electrode, which seems related to particle cracking due to mechanical stresses. A high-temperature effect seems to add upon this low-temperature baseline, introducing further SEI growth and possible instability of the positive electrode structure. This interpretation is the consequence of the superposition effect that rules at thermodynamic level.

Conclusions

A wide experimental campaign is conducted to reproduce a realistic operation of lithium-ion batteries in BEVs and investigate the effect of the operating conditions. These are identified after a relevant literature review, to highlight the most common conditions. In particular, WLTP is selected as representative load profile and converted into power-time profile with a simplified vehicle model, after benchmarking its characteristics with a local driving schedule, and compared against the standard IEC 62660–1.

Characterization tests are performed periodically to track the

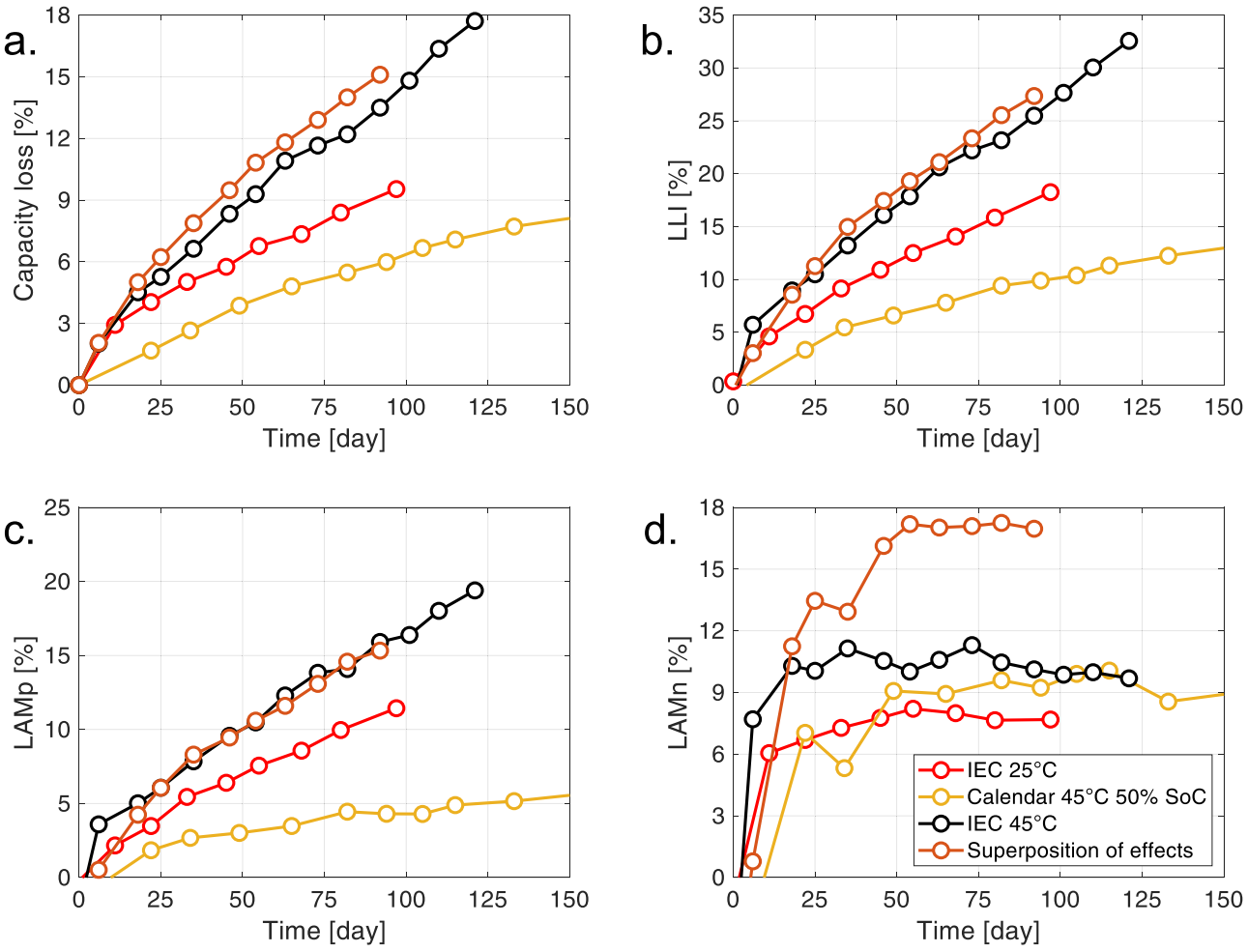

Fig. 11. Superposition effect of low temperature cycling and high temperature calendar ageing. Comparison of a) capacity loss, b) LLI, c) LAMp and d) LAMn for three cells: IEC cycle at 25 °C (red curves), calendar ageing at 45 °C and 50 % SoC (yellow) and IEC cycle at 45 °C (black). The sum of the first two is reported in orange.

residual performance and perform capacity loss and thermodynamic analyses. One sample is investigated as a reference, observing the following trends.

- Loss of lithium inventory is detected as the main degradation parameter. It can be related to both SEI growth but also other mechanisms like loss of lithiated electrode material. Indeed, both negative and positive electrode are affected by LAM.
- LAMn is found to be very steep in the first cycles and then stabilizes. It can be associated with a stabilization of the material, uncorrelated with the operating conditions, but it can also explain the sudden drop of capacity in the first cycles as a lithiated LAMn. On the contrary, LAMp is linear over EFC.

Differences among different samples are then analysed to highlight the role of the operating conditions.

- Surprisingly, different load profile do not induce significant differences in capacity loss rate and thermodynamic parameters. Similarly, C/6, C/3 and 1 C recharge rates do not affect the degradation rates.
- There is a strong proportionality between LAMp and DoD, which supports a mechanical origin of this parameter: the larger the DoD, the larger the volume variations which, in turn, induce particle cracking. LLI has a complex interdependence on SoC and DoD.

Interestingly, the superposition principle is shown to hold true for thermodynamic ageing parameters, where LLI and LAMp of a high temperature cycle are reproduced by the sum of the corresponding parameters of the low temperature cycle and the contribution of calendar ageing at high temperature, at the average SoC of the cycle. All in all, higher temperatures introduce further SEI growth and deterioration of the positive electrode, maybe transition metal dissolution. Additional investigations on the operation far from equilibrium will be the topic of a forthcoming publication, together with ex-situ measurements to verify the reliability of the interpretations.

CRediT authorship contribution statement

Gabriele Sordi: Writing – review & editing, Writing – original draft, Visualization, Validation, Methodology, Investigation, Formal analysis, Data curation, Conceptualization. **Andrea Rondi:** Visualization, Investigation, Formal analysis, Conceptualization. **Davide Conti:** Visualization, Investigation, Formal analysis, Conceptualization. **Andrea Casalegno**: Writing – review & editing, Supervision, Project administration, Funding acquisition. **Claudio Rabissi:** Writing – review & editing, Supervision, Project administration, Funding acquisition, Conceptualization.

Declaration of Competing Interest

The authors declare that they have no known competing financial

interests or personal relationships that could have appeared to influence the work reported in this paper.

Data Availability

Data will be made available on request.

Acknowledgements

This work was supported by the European Union's Horizon 2020 Research and Innovation Program [Grant Agreement No. 873111, project "DigiPrime - Digital Platform for Circular Economy in Cross-sectorial Sustainable Value Networks"] and the Energy for Motion initiative of Politecnico di Milano as part of Energy department recognition as Department of Excellence 2018–2020 from Italian Ministry of Education, Universities and Research (MIUR).

The authors would like to acknowledge Andrea Stecchini and Roberto Evangelista for their support in the experimental campaign at 25 °C.

Appendix A. Supporting information

Supplementary data associated with this article can be found in the online version at doi:10.1016/j.fub.2024.100005.

References

[1] G. Sordi, C. Rabissi, A. Casalegno, Energ. (Basel) 16 (2023), https://doi.org/10.3390/en16124730.
[2] C. Rabissi, G. Sordi, A. Innocenti, A. Casalegno, J. Energy Storage 59 (2023), https://doi.org/10.1016/j.est.2022.106435.
[3] G. Sordi, M. Sedzik, A. Casalegno, C. Rabissi, Diagnosis of lithium-ion batteries degradation with P2D model parameters identification: a case study on low temperature charging, Under Review (n.d.).
[4] G. Sordi, D. Luder, W. Li, D.U. Sauer, A. Casalegno, C. Rabissi, Investigation of calendar ageing of lithium-ion battery through physical models with ex-situ validation, Under Review (n.d.).
[5] J. Kim, J. Oh, H. Lee, Appl. Therm. Eng. 149 (2019) 192–212, https://doi.org/10.1016/j.applthermaleng.2018.12.020.
[6] T.M. Bandhauer, S. Garimella, T.F. Fuller, J. Electrochem Soc. 158 (2011) R1, https://doi.org/10.1149/1.3515880.
[7] P.R. Tete, M.M. Gupta, S.S. Joshi, J. Energy Storage 35 (2021), https://doi.org/10.1016/j.est.2021.102255.
[8] J. Smart, S. Schey, SAE Int. (2012) 27–33, https://doi.org/10.4271/2012-01-0199.
[9] C. Corchero, European electric vehicle fleet: driving and charging behaviors, n.d.
[10] J. Yang, J. Dong, Q. Zhang, Z. Liu, W. Wang, Transp. Res Rec. 2672 (2018) 20–30, https://doi.org/10.1177/0361198118759015.
[11] Y. Zou, S. Wei, F. Sun, X. Hu, Y. Shiao, Energy 100 (2016) 25–39, https://doi.org/10.1016/j.energy.2016.01.062.
[12] L. Hu, J. Dong, Z. Lin, Transp. Res Part C. Emerg. Technol. 102 (2019) 474–489, https://doi.org/10.1016/j.trc.2019.03.027.
[13] NOW GMBH, Elektromobilitaet in der Praxis, 2020.
[14] A. Tomaszewska, Z. Chu, X. Feng, S. O'Kane, X. Liu, J. Chen, C. Ji, E. Endler, R. Li, L. Liu, Y. Li, S. Zheng, S. Vetterlein, M. Gao, J. Du, M. Parkes, M. Ouyang, M. Marinescu, G. Offer, B. Wu, ETransportation 1 (2019), https://doi.org/10.1016/j.etran.2019.100011.
[15] S. Saxena, D. Roman, V. Robu, D. Flynn, M. Pecht, Energ. (Basel) 14 (2021), https://doi.org/10.3390/en14030723.
[16] P. Keil, A. Jossen, J. Electrochem Soc. 164 (2017) A3081–A3092, https://doi.org/10.1149/2.0801713jes.
[17] G. Baure, M. Dubarry, Batteries 5 (2019), https://doi.org/10.3390/batteries5020042.
[18] S. Khan, S. Shariff, A. Ahmad, M. Saad Alam, Smart Sci. 6 (2018) 271–293, https://doi.org/10.1080/23080477.2018.1488205.
[19] I. Energy Agency, Global EV Outlook 2024 Moving towards increased affordability, 2024. ⟨www.iea.org⟩.
[20] G.M.S. De Andrade, F.W.C. De Araújo, M.P.M. De, Novaes Santos, F.S. Magnani, Energ. (Basel) 13 (2020), https://doi.org/10.3390/en13205434.
[21] J. Brady, M. O'Mahony, Appl. Energy 177 (2016) 165–178, https://doi.org/10.1016/j.apenergy.2016.05.094.
[22] L. Joud, R. Da Silva, D. Chrenko, A. Kéromnès, L. Le Moyne, Energ. (Basel) 13 (2020), https://doi.org/10.3390/en13112954.
[23] A. Tourani, P. White, P. Ivey, J. Power Sources 268 (2014) 301–314, https://doi.org/10.1016/j.jpowsour.2014.06.010.
[24] Y. Tripathy, A. McGordon, C.T.J. Low, Energ. (Basel) 11 (2018), https://doi.org/10.3390/en11092439.
[25] M. Pfriem, F. Gauterin, World Electr. Veh. J. 8 (2016) 14–24.
[26] J.I. Huertas, L.F. Quirama, M. Giraldo, J. Díaz, Energ. (Basel) 12 (2019), https://doi.org/10.3390/en12040665.
[27] Iddo Riemersma - Sidekick Project Support, Technical Report on the development of a World-wide Worldwide harmonised Light duty driving Test Procedure (WLTP), n.d.
[28] British Standard Institution, Secondary lithium-ion cells for the propulsion of electric road vehicles, 2019.
[29] P. Keil, A. Jossen, World Electr. Veh. J. 7 (2015) 41–51.
[30] C. Fiori, K. Ahn, H.A. Rakha, Appl. Energy 168 (2016) 257–268, https://doi.org/10.1016/j.apenergy.2016.01.097.
[31] Argonne National Laboratory, D3 2014 BMW i3BEV, ⟨Https://Www.Anl.Gov/Taps/D3–2014-Bmw-I3bev⟩ (2021).
[32] I. Evtimov, R. Ivanov, M. Sapundjiev. in: MATEC Web of Conferences, EDP Sciences, 2017, https://doi.org/10.1051/matecconf/201713306002.
[33] S. Shahidinejad, E. Bibeau, S. Filizadeh, IEEE Trans. Veh. Technol. 59 (2010) 3710–3719. ⟨https://doi.org/10.1109/TVT.2010.2061243⟩.
[34] Sony Energy Devices Corporation, Lithium Ion Rechargeable Battery Technical Information Model US18650V3, 2011.
[35] C. Pastor-Fernández, K. Uddin, G.H. Chouchelamane, W.D. Widanage, J. Marco, J. Power Sources 360 (2017) 301–318, https://doi.org/10.1016/j.jpowsour.2017.03.042.
[36] J. Stadler, C. Krupp, M. Ecker, J. Bandlow, B. Spier, A. Latz, J. Power Sources 521 (2022), https://doi.org/10.1016/j.jpowsour.2021.230952.
[37] P. Shafiei Sabet, A.J. Warnecke, F. Meier, H. Witzenhausen, E. Martinez-Laserna, D. U. Sauer, J. Power Sources 449 (2020), https://doi.org/10.1016/j.jpowsour.2019.227369.
[38] J. Wandt, A. Freiberg, R. Thomas, Y. Gorlin, A. Siebel, R. Jung, H.A. Gasteiger, M. Tromp, J. Mater. Chem. A Mater. 4 (2016) 18300–18305, https://doi.org/10.1039/C6TA08865A.
[39] S.J. An, J. Li, C. Daniel, D. Mohanty, S. Nagpure, D.L. Wood, Carbon N. Y 105 (2016) 52–76, https://doi.org/10.1016/j.carbon.2016.04.008.
[40] J.S. Edge, S. O'Kane, R. Prosser, N.D. Kirkaldy, A.N. Patel, A. Hales, A. Ghosh, W. Ai, J. Chen, J. Yang, S. Li, M.C. Pang, L. Bravo Diaz, A. Tomaszewska, M. W. Marzook, K.N. Radhakrishnan, H. Wang, Y. Patel, B. Wu, G.J. Offer, Phys. Chem. Chem. Phys. 23 (2021) 8200–8221, https://doi.org/10.1039/d1cp00359c.
[41] C.R. Birkl, M.R. Roberts, E. McTurk, P.G. Bruce, D.A. Howey, J. Power Sources 341 (2017) 373–386, https://doi.org/10.1016/j.jpowsour.2016.12.011.
[42] S. Schindler, M.A. Danzer, J. Power Sources 343 (2017) 226–236, https://doi.org/10.1016/j.jpowsour.2017.01.026.
[43] M. Dubarry, C. Truchot, B.Y. Liaw, J. Power Sources 219 (2012) 204–216, https://doi.org/10.1016/j.jpowsour.2012.07.016.
[44] A.J. Smith, P. Svens, M. Varini, G. Lindbergh, R.W. Lindström, J. Electrochem Soc. 168 (2021) 110530, https://doi.org/10.1149/1945-7111/ac2d17.
[45] J. Schmalstieg, S. Käbitz, M. Ecker, D.U. Sauer, J. Power Sources 257 (2014) 325–334, https://doi.org/10.1016/j.jpowsour.2014.02.012.
[46] J. Wang, J. Purewal, P. Liu, J. Hicks-Garner, S. Soukazian, E. Sherman, A. Sorenson, L. Vu, H. Tataria, M.W. Verbrugge, J. Power Sources 269 (2014) 937–948, https://doi.org/10.1016/j.jpowsour.2014.07.030.
[47] T. Raj, A.A. Wang, C.W. Monroe, D.A. Howey, Batter. Batter. Supercaps 3 (2020) 1377–1385, https://doi.org/10.5287/bodleian:v0ervBv6p.